Real-Time X-ray Scattering Discovers Rich Phase Behavior in PbS Nanocrystal Superlattices during *In Situ* Assembly

*Irina Lokteva**[†‡], Michael Dartsch[†‡], Francesco Dallari[†], Fabian Westermeier[†], Michael Walther[†], Gerhard Grübel[†‡], and Felix Lehmkühler[†‡]*

[†] Deutsches Elektronen-Synchrotron DESY, Notkestr. 85, 22607 Hamburg, Germany

[‡] The Hamburg Centre for Ultrafast Imaging (CUI), Luruper Chaussee 149, 22761 Hamburg, Germany

*E-mail: irina.lokteva@desy.de

ABSTRACT

During the self-organization of colloidal semiconductor nanoparticles by solvent evaporation, nanoparticle interactions are substantially determined by the organic ligands covering the inorganic core. However, the influence of the ligand grafting density on the assembly pathway is often not considered in experiments. Here, we carry out an *in-situ* synchrotron small angle X-ray scattering and X-ray cross-correlation analysis study of the real-time assembly of oleic acid-capped PbS nanocrystals at a low ligand coverage of 2.7 molecules/nm^2. With high temporal and spatial resolution, we monitor the transitions from the colloidal suspension through the solvated superlattice states into the final dried superstructure. In a single *in situ* experiment, we observe a two-dimensional hexagonal, hexagonal close-packed, body-centered cubic, body-centered tetragonal (with different degree of the tetragonal distortion), and face-centered cubic superlattice phases. Our results are compared to the self-organization of PbS nanocrystals with a higher ligand coverage up to 4.5 molecules/nm^2, revealing different assembly pathways. This highlights the importance of determination of the ligand coverage in assembly experiments in order to approach a complete understanding of the assembly mechanism as well as to be able to predict and to produce the targeted superstructures.

INTRODUCTION

Colloidal semiconductor nanocrystals (NCs) represent a promising material for a wide range of technological applications due to their monodispersity, ease of handling and tunable optical properties by the particle size. The ability of colloidal NCs to form ordered structures *via* self-assembly, *e.g.*, upon solvent evaporation or destabilization using a non-solvent, is an attractive way to obtain so called "superlattices" that, besides displaying the unique physical and chemical properties of individual NCs, exhibit novel collective properties as a result of the strong delocalization and electronic coupling between well-arranged nanoparticle layers. Typically, widespread wet chemical synthesis methods yield colloidal NCs covered by a stabilizing surfactant layer of organic ligands, which acts to solubilize the NCs in the desired organic medium and is directly involved in the assembly process. Whereas various parameters are known to affect the structure of the self-assembled NC superlattice in a solvent-mediated assembly, such as, *e.g.*, the rate of solvent evaporation and hence superlattice crystallization, NC core composition, size and shape, NC concentration, type of ligand and solvent used *etc.*,[1-3] the relationship between the ligand grafting density and the obtained superlattice structure is still poorly understood.

For potential electronic or optoelectronic applications, as-synthesized colloidal lead sulfide (PbS) NCs with the commonly used oleic acid ligands require a thorough purification, which is in particular necessary to ensure success of the consequent ligand exchange.[4,5] During the post-synthesis processing of semiconductor NCs, multiple parameters, such as the precise composition and stoichiometry of NCs depending on the synthesis protocol, the exact washing procedure (amount of precipitation steps and solvents used) as well as the storage conditions influence the surface chemistry, which is why the ligand grafting density varies from sample to sample.[6-9] For PbS NCs a variety of superlattice structures has been reported, such as a face-centered cubic

(FCC), hexagonal closed-packed (HCP), body-centered cubic (BCC), and body-centered tetragonal (BCT)[9-16] and only a few experimental studies considered the impact of the ligand coverage of typically used ligands, *e.g.*, oleic acid, on the final superlattice state.[8,17] Due to the faceted nature of lead chalcogenide NC cores and the different binding energy of oleic acid molecules to the $\{100\}_{NC}$ and $\{111\}_{NC}$ facets,[18-21] the ligand grafting density might additionally influence the anisotropy of a ligated nanocrystal and becomes an essential parameter that needs to be taken into account for the desired assembly outcome.[8,9,17] Moreover, it has been demonstrated that different structures of binary NC superlattices consisting of PbS and Au NCs formed depending on the oleic acid coverage of PbS NCs.[22]

The origin of a certain superlattice configuration for the case of PbS NCs is still a subject of ongoing research, because even at seemingly similar conditions different self-assembled superlattice structures have been observed.[16,23] The recently emerged *in situ* X-ray scattering methods of the self-assembly characterization represent a promising route for providing insights into the assembly mechanism and uncover the time-resolved superlattice transitions.[24-27] However, the discussion and determination of the ligand grafting density is often absent in literature, which complicates comparison between experimental results obtained for similar systems in independent investigations and hinder development of theoretical models that would help navigating the assembly pathway to produce the targeted superlattices.

Here, we aim to investigate the NC self-assembly on the example of faceted oleic acid-capped PbS NCs (8.2 nm in diameter) dispersed in heptane using a combination of controlled solvent evaporation and *in situ* synchrotron small-angle X-ray scattering (SAXS). We analyze the time-resolved superlattice structures with high temporal resolution and, by determining the surface ligand coverage of PbS NCs, try to elucidate the role of ligand grafting density in the assembly

process. In particular, we show that the lower density of oleic acids ligands of approx. 2.7 molecules/nm^2 in this study and the higher ligand grafting density up to 4.5 molecules/nm^2 from ref 28 result in different self-assembled structures at all other conditions, *i.e.*, synthesis, post-synthesis processing, and self-assembly environment, kept the same. The measurement is performed in transmission SAXS geometry, which allows us to obtain the SAXS signal over the whole volume of the colloidal suspension and, during controlled solvent evaporation, over the whole thickness of the self-assembled film. Thus, the structural information of the bulk suspension/superlattice volume can be accessed. In addition to the conventional SAXS analysis, where the scattering data are averaged along an azimuthal ring of a two-dimensional pattern and thus some structural information might be lost, we perform the X-ray cross-correlation analysis (XCCA) of the real-time SAXS data. This allows us to gain insights into the subtle structural changes of the superlattice states and decipher some details that uncover the assembly mechanism.

EXPERIMENTHAL SECTION

Synthesis of Oleic Acid-Capped PbS Nanocrystals

The PbS nanocrystals were synthesized by the hot-injection method of Hines and Scholes.[29] Concisely, 0.759 g of lead acetate trihydrate (99.999% Sigma Aldrich) and 20 ml of oleic acid (90%, Sigma Aldrich) were placed in a three-neck round-bottom flask and heated at 120 °C for 1 hour under reduced pressure of 2.5x10^{-1} mbar. Subsequently, the reaction solution was purged with argon and heated up to 147 °C. In a nitrogen glovebox, a syringe was prepared containing 0.210 ml of bis(trimethylsilyl)sulfide (Sigma Aldrich) dissolved in 10 ml of dried octadecene (90% Sigma Aldrich). The content of the syringe was rapidly injected into the colorless reaction solution with a G14 needle at approx. 145 °C under constant stirring. The heating mantle was removed

before the injection. After nanoparticle growth for the duration of 3 min the reaction was stopped by quenching by a cold water bath and the suspension was allowed to cool down to room temperature. The colloidal suspension was mixed with hexane and the particles were precipitated with ethanol by centrifuging at 8,000 rpm for 5 min. Afterwards, the supernatant was removed and the particles were redispersed in hexane. The purifying procedure was repeated three more times (size-selective precipitation was applied during the second precipitation step) and the washed particles were redispersed in anhydrous heptane (Sigma Aldrich). Overall, the particles have been precipitated four times after the synthesis. It has to be noted that at this step nanoparticles could be well suspended in heptane, whereas one more additional precipitation step removed too many ligands and resulted in an inhomogeneous nanoparticle suspension. The PbS NC suspension in heptane after 4 washing cycles was stored in a dry nitrogen glovebox at the concentration of 74 mg/ml. The concentration of PbS NC suspension in heptane for the *in situ* self-assembly experiment was chosen to be 10 mg/ml in order to obtain well-ordered nanocrystal superlattices with sufficient SAXS signal and to avoid multiple scattering in solution, which becomes an issue at concentrations larger than 30 mg/ml.[7]

In Situ **Small-Angle X-ray Scattering upon Controlled Solvent Evaporation**

The *in situ* SAXS measurements were performed at the P10 Coherence Applications Beamline of the synchrotron radiation source PETRA III, Hamburg, Germany. The energy of the incident X-ray beam was set to 13.0 keV and the beam size was 2 µm (v) x 3 µm (h). The SAXS data were collected using an EIGER X4M detector at 5.039 m sample-to-detector distance and a typical exposure time of 0.2 s. Two-dimensional SAXS patterns were azimuthally integrated into one-dimensional scattering curves $I(q)$ presented as a function of scattering vector $q = \frac{4\pi}{\lambda}\sin\left(\frac{\theta}{2}\right)$,

where λ = 0.0954 nm is the wavelength of the incident X-ray beam and θ is the scattering angle. The *I(q)* of the particle form factor of the colloidal nanocrystals was corrected for the background scattering of the solvent and the experimental setup. It has to be noted that no radiation damage of the sample was observed for the chosen exposure times.

The real-time self-assembly of PbS nanocrystals was monitored during controlled solvent evaporation in a custom-built chamber.[30] In brief, the solvent vapor chamber (inner volume approx. 72 cm^3) used for *in situ* SAXS measurements was equipped with two Kapton windows for the incident and scattered X-ray beam. The chamber was evacuated and purged with helium to remove oxygen and water content. After that the chamber was saturated with pure solvent (27 µl of heptane). Subsequently, the nanoparticle suspension in heptane was injected into the inner liquid sample cell, consisting of two silicon nitride membranes at 0.5 mm separation (membrane size of 5 mm x 5 mm and thickness of 500 nm). The helium flow through the chamber was started at a controlled rate of 1.8 cm^3/min, allowing for the slow solvent evaporation from the colloidal suspension (volume ≈ 24.5 µl). The evaporation rate was 0.25 µl/min for the nanoparticle suspension in heptane. During all measurements the cell temperature was kept constant at 23–25 °C. The start of the experimental time was defined by turning on the helium flow inside the experimental hutch. The hutch was searched and the beginning of measurements was initiated at 3 min of elapsed time. The absolute time of solvent evaporation depends additionally on the solvent saturation level and the filling level of the colloidal suspension. Thus, evaporation times presented in this paper should be considered from the relative-to-each-other point of view rather than absolutely.

The SAXS data during the *in situ* solvent evaporation of a 10 mg/ml PbS NC colloidal suspension were recorded by scanning over three horizontal and nine vertical positions on the silicon nitride

windows to ensure adequate statistics and reasonable time resolution of around 1.4 min at each measurement point. The form factor fit of the *I(q)* of the PbS NC colloidal suspension in heptane preceding the superlattice formation was carried out using the Schulz–Flory distribution for dispersed spheres.

Nanoparticle Characterization

Transmission Electron Microscopy (TEM) images were acquired using a JEOL JEM-1011 instrument operating at 100 kV. To prepare the TEM sample, a drop of the diluted NC solution in heptane was deposited on a carbon-coated copper grid and dried in air.

UV-Vis-NIR absorbance measurements were recorded using PbS NCs dissolved in tetrachloroethylene at a Varian Cary 5000 spectrometer.

Thermogravimetric analysis (TGA) was performed on a Netzsch TG 209 F1 Iris instrument. 7.667 mg of PbS NCs in an alumina crucible was heated up to 600 °C at a rate of 10 °C/min under nitrogen atmosphere. Baseline correction was performed by running TGA on an empty crucible under the same experimental conditions.

Scanning electron microscopy (SEM) was carried out using a LEO 1550 Gemini instrument at 2-20 kV for the imaging of self-assembled superlattice films after the *in situ* SAXS measurements.

RESULTS AND DISCUSSION

For the investigation of the *in-situ* assembly of colloidal NCs into highly ordered superlattices upon controlled solvent evaporation, we use a dedicated sample environment.[28,30,31] Briefly, in a solvent vapor saturated atmosphere the colloidal suspension of PbS NCs, *e.g.*, in heptane, is filled into a cell consisting of two X-ray transparent silicon nitride membranes at a narrow separation (**Figure 1a**). Afterwards, the slow evaporation of the solvent from the colloidal suspension – the

evaporation rate for heptane is ~0.25 µl/min (**Figure S1**) – is initiated by a helium gas flow through the chamber (for details see Experimental Section). PbS NCs self-assemble into ordered superlattice films under quasi-equilibrium conditions along the silicon nitride cell windows during the movement of the evaporation front (**Figure 1b**).

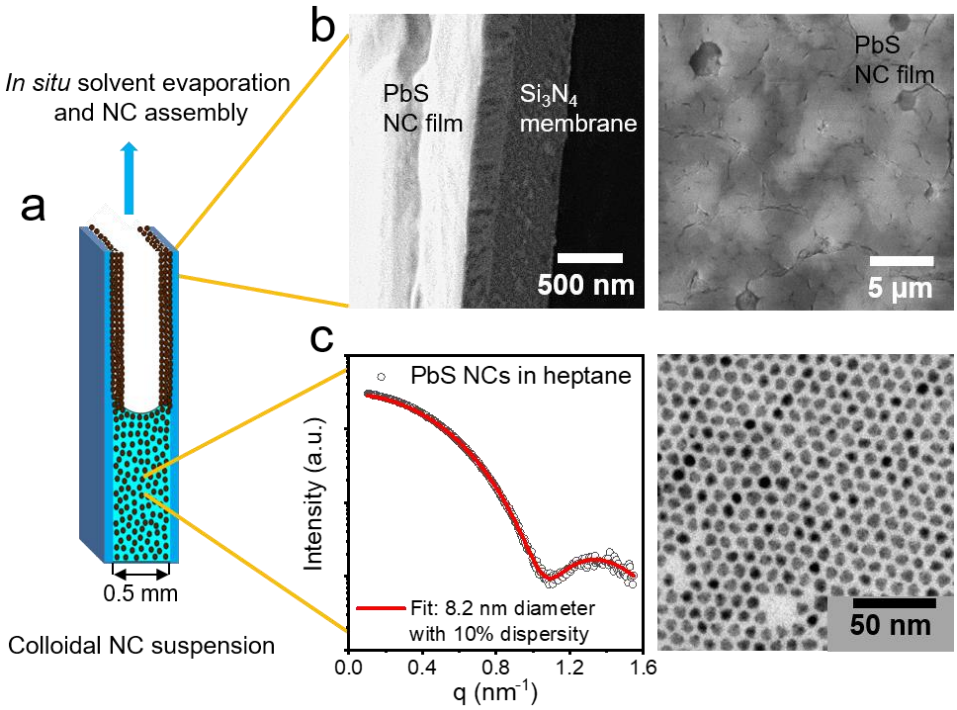

Figure 1. *In situ* self-assembly of PbS NCs: (a) Schematic representation of the sample cell with PbS NC suspension during *in situ* solvent evaporation. The SAXS patterns are acquired in transmission geometry through the silicon nitride membranes, which serve as the cell walls during real-time NC assembly. NCs form highly ordered superlattice films along the silicon nitride windows. (b) SEM images of the post-assembly NC films in side (left) and front (right) view. (c) Azimuthally integrated SAXS curve of the colloidal suspension in the beginning of the self-assembly with the corresponding form factor fit (left) and TEM image of PbS NCs obtained from the colloidal suspension used for the *in situ* SAXS experiments (right).

In our previous study, we investigated the real-time self-organization of oleic acid-functionalized 7.8 nm sized PbS NCs (with 10% size dispersity) and exhibiting a high ligand coverage of 4.5 molecules/nm^2 estimated assuming a cuboctahedral-shaped NC core (obtained after 2 washing cycles).[28] To observe the effect of the ligand coverage on the self-organized NC superlattice, in this study we utilize well-purified (4 washing cycles, see Experimental Section) oleic acid-stabilized 8.2 nm in diameter (with 10% size dispersity) PbS NCs dispersed in heptane as a sample system (**Figure 1c**). Such degree of purification is typically applied to semiconductor nanoparticles for the subsequent utilization in optoelectronic device fabrication.[32,33] At this point, it has to be noted that after 4 washing cycles the NCs could be still well suspended in heptane, whereas one more additional precipitation step resulted in ligand-deficient nanoparticles that could not be redispersed homogeneously in the corresponding solvent. The ligand grafting density of PbS NCs after 4 washing cycles was determined using the thermogravimetric analysis to be 2.71 ± 0.27 molecules/nm^2 considering a cuboctahedral shape of the inorganic core (for details see Supporting Information and **Figure S2**). The error in this estimate results from the error in the diameter determination of NCs and its dispersity (Figure 1c). For the SAXS and TGA measurements, the same batch of NCs has been used. For the subsequent discussion, we use the value of 2.7 molecules/nm^2 as the average estimate of the ligand coverage. In view of recent findings in ref 7, we estimate that such well-purified NCs after 4 steps of the precipitation-redispersion possess a ligand density which is close to the monolayer coverage for oleic acid molecules (see considerations in the Supporting Information). In other words, we suppose that the fraction of free and/or physiosorbed oleic acid ligands is low for this particular sample and can be neglected during further discussion.

Because ligands exhibit different solvation in different solvents,[34] the choice of the solvent is expected to determine ligand-solvent interactions during the assembly process. It has to be noted that in ref 28 both heptane and toluene were used as a solvent for the NC suspension applied for the *in situ* self-assembly, whereas no difference in the superlattice structures has been observed for these two solvents. Due to better ordering of NCs in heptane,[28] in this study we utilize only heptane as solvent. In addition, it has been recently demonstrated that not only the choice of the ligand influences the ligand grafting density of NCs but also the concrete processing and purification procedure of NCs after the synthesis (including washing steps and solvents used).[6,7] In this respect, we note that the same purification procedure with the same solvents has been applied in ref 28 and in this study, with the only difference of 2 *versus* 4 washing cycles.

As it can be seen from the post-assembly scanning electron microscopy (SEM) images (Figure 1b), the obtained NC superlattice film (upon evaporation from a 10 mg/ml PbS NC suspension in heptane) has a thickness of approximately 200 nm, which corresponds to about 19–20 monolayers of PbS NCs considering the ligand shell thickness (see following considerations in this paper). This confirms the three-dimensional structure of the self-assembled superlattice. The front view of the self-crystallized PbS superlattice film (Figure 1b) reveals large domain sizes of up to several micrometers. For the *in situ* SAXS measurements, we employ a coherent X-ray beam at beamline P10 of the PETRA III synchrotron facility with a beam size of approximately 2 x 3 μm^2 (vertical x horizontal). Such a focused beam allows for the observation of the superlattice transitions with high spatial resolution.

During the *in situ* self-assembly of PbS NCs upon controlled solvent evaporation, the SAXS patterns were acquired on a grid of 3 horizontal and 9 vertical positions as shown in **Figure 2a**, so that a time resolution of 1.4 min was achieved at each measurement point. The results presented

throughout this paper were acquired at the measurement point denoted by a red dot in Figure 2a. It has to be noted that at other measurement points the same superlattice transitions and the final superlattices with the same lattice parameters were observed with absolute time values depending on the vertical position. Some differences have arisen at the bottom points due to the higher NC concentration in the remaining liquid of the suspension, which is out of the scope of this paper due to the lack of statistics and reproducibility.

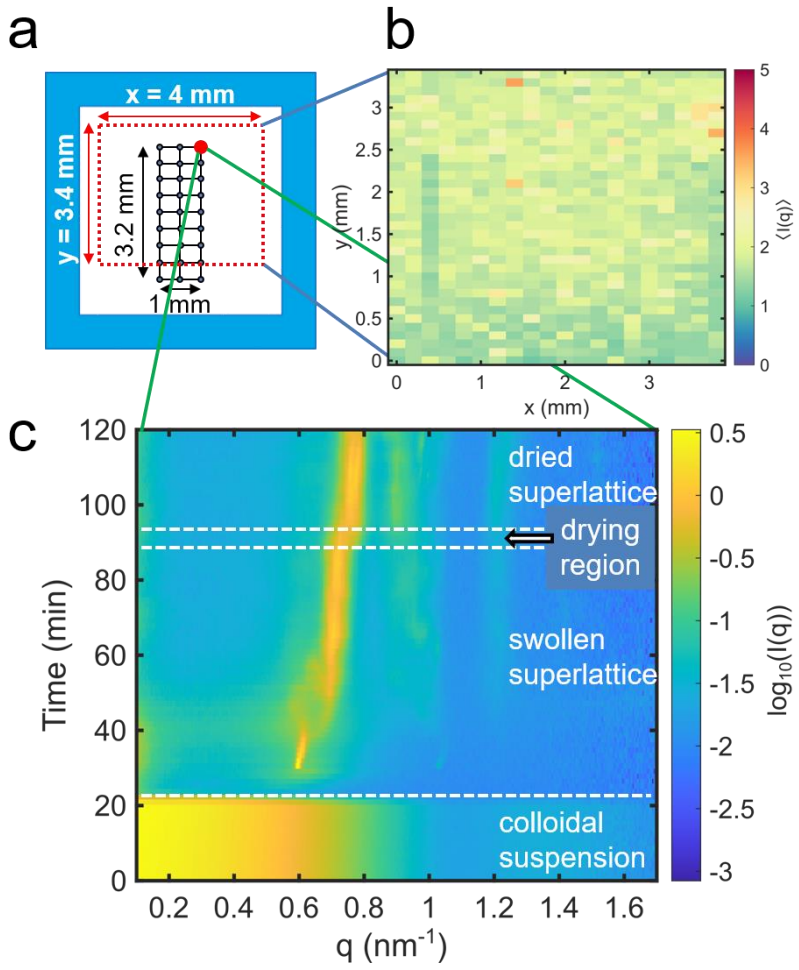

Figure 2. Transmission SAXS measurements: (a) Scheme of the side view of the silicon nitride cell windows with typical measurement points during the *in situ* self-assembly. The red dashed line shows the region of the SAXS scan performed on the dried superlattice, represented in (b). (b) Total integrated intensity map of the dried superlattice after the *in situ* self-assembly took place. (c) Temporal evolution of SAXS curves, obtained by the azimuthal integration of 2D SAXS

patterns, during the *in situ* self-assembly of colloidal PbS NCs into superlattices upon solvent evaporation acquired at the point shown in red in (a).

After the NC self-assembly had taken place, dried NC superlattice films were scanned over a larger area as shown by the dotted red rectangle in Figure 2a with a spatial resolution of 200 µm horizontally and 100 µm vertically to obtain better statistics of the final NC superlattice. As it can be seen from **Figure 2b**, the map of the total integrated intensity of the SAXS signal is quite homogeneous in the measured region. Additional optical microscopy images of the self-assembled NC film can be found in **Figure S3**.

Figure 2c depicts the temporal evolution of the azimuthally integrated SAXS signal during the *in situ* self-assembly upon solvent evaporation from a 10 mg/ml PbS NC suspension in heptane. The following regimes of the assembly states can be identified: the colloidal suspension, the swollen superlattice state (with evident superlattice transitions within this phase), the drying region of the self-organized superlattice, and finally the dried superlattice, where no further solvent evaporation is observed. The superlattice transitions from the wet to the dry state for PbS NC superlattices have been also reported in other *in situ* studies,[16,35] yet the role of the complex ligand-solvent and ligand-ligand interactions is still poorly understood. In this work, due to the very slow and controlled solvent evaporation under quasi equilibrium conditions we are able to capture several phases in the solvated superlattice state and due to the simultaneous measurement of different vertical points we determine the moment of evaporation of solvent molecules from the interstitial sites of the wet superlattice, which allows us to resolve the assembling process in more detail.

The analysis of the time-resolved SAXS curves during the *in-situ* NC assembly shown in Figure 2c is presented in **Figure 3** for selected times. The start of the experimental time of the assembly process was defined by the start of the helium flow through the evaporation chamber, the exact

time evolution depends on the volume of the colloidal suspension and the amount of the solvent used for the chamber saturation.

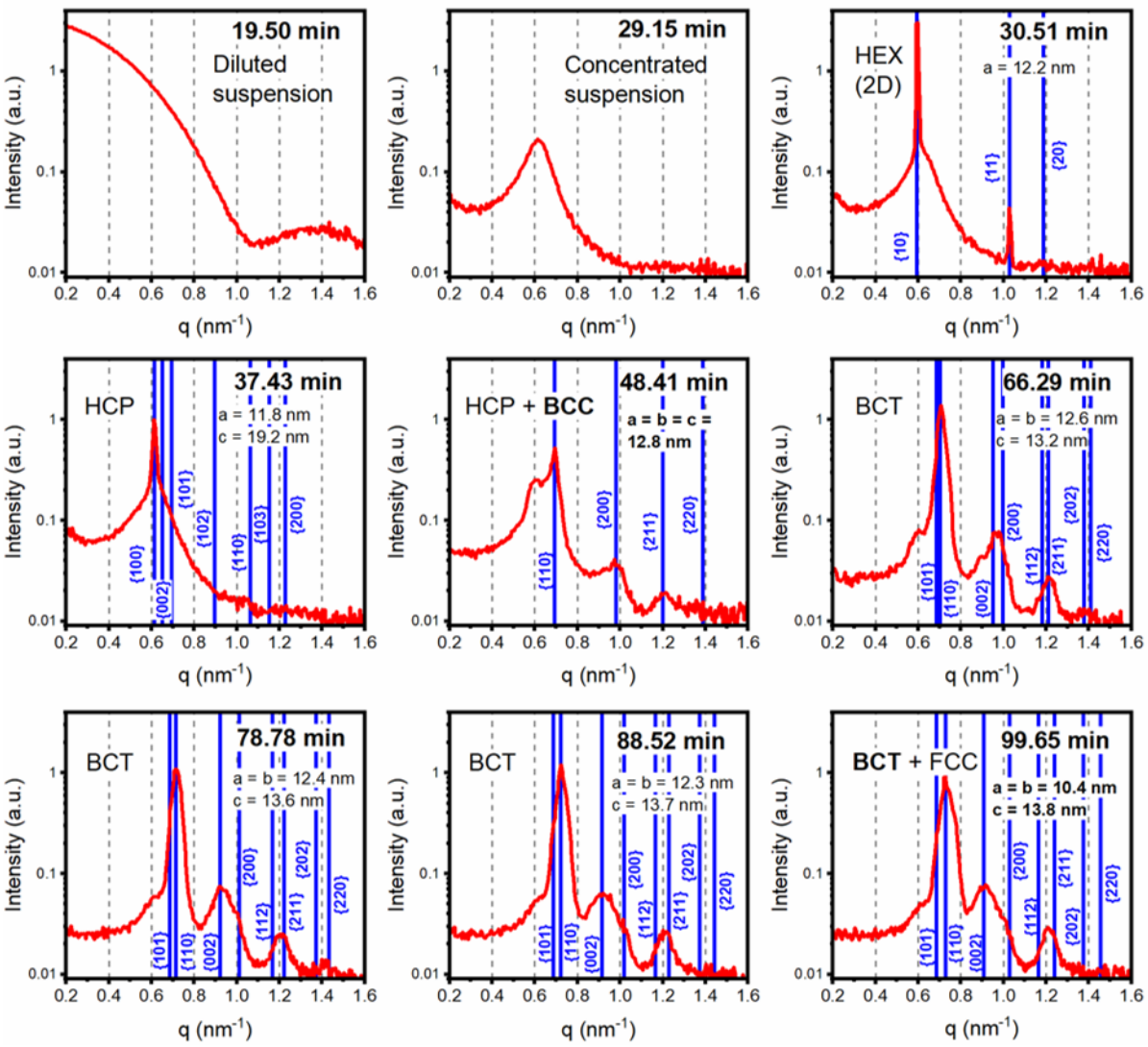

Figure 3. Tracking representative superlattice phase behavior. SAXS curves during *in situ* self-assembly of colloidal PbS NCs at chosen time values show the superlattice structure formation and transitions. The solvent evaporation from the swollen crystallized superlattice starts at approx. 89 min of elapsed time and continues up to approx. 96 min of elapsed time. The predominant superlattice phases during the coexistence of different lattice structures are indicated in bold. The positions of the Bragg peaks are shown for the corresponding dominating superlattices in the case of phase coexistence.

In the first 20 min of solvent evaporation, the SAXS signal of a colloidal suspension of not ordered particles is observed. At this stage, the SAXS curve can be well described by a single form factor of spherical particles (Figure 1c). Upon controlled solvent evaporation, the NC concentration increases and at 30.51 min the formation of a hexagonal (HEX) superlattice is evident. Most probably, at this stage the hexagonal superlattice is two-dimensional (2D), as it can be seen from the fit in Figure 3 which gives a lattice constant a = 12.2 nm. During further solvent evaporation, we observe a change of the hexagonal superlattice, namely a decrease of the intensity of the first peak with simultaneous broadening (which corresponds to the $\{10\}_{2D\ HEX}$ or the $\{100\}_{HCP}$ reflection) and shift towards larger q values, as shown in **Figure S4**. In addition, the Bragg peak of the $\{11\}_{2D\ HEX}$ reflection widens and becomes less pronounced, which indicates that the crystallite size decreases. Assuming that the 2D HEX structure transfers into the three-dimensional one, we show a fit using the HCP reflections in Figure 3 at 37.43 min. This is in accordance with our previous publication ref 23, where the HCP superlattice with the same lattice parameters (a = 11.8 nm and $c = \sqrt{\frac{8}{3}}a$) in the beginning of the self-assembly was detected. Moreover, the thickness of the final self-assembled film of 19-20 monolayers exceeds the number of layers, for which typically a 2D HEX structure can be modeled.[36]

At 38.80 min, the BCC superlattice starts to evolve from the hexagonal superlattice with the lattice constant $a = b = c =$ 12.9 nm and becomes predominant at 48.41 min ($a = b = c =$ 12.8 nm) with the HCP superlattice still present, evident by a peak at q = 0.61 nm^{-1} (Figure 3 and **Figure 4a**). This observation is in accordance with our findings reported in ref 28. Furthermore, in recent grazing-incidence as well as tangential and normal incident SAXS studies of the *in situ* self-assembly of PbS NCs by means of the printing deposition and antisolvent diffusion, the coexistence of the FCC (or FCC/HCP) and BCC phases in the self-organized superlattice has been

reported.[35,37] Due to the very similar free energy of the FCC and HCP structures both are equally probable to occur.[38-41] It has to be noted that the peak/shoulder at q = 0.61 nm^{-1} originating from the hexagonal superlattice remains present in the SAXS curves obtained by the azimuthal integration of 2D scattering patterns during the whole assembly process until the final dried state at 99.65 min (Figure 3).

Using XCCA,[42] we analyze the 2D SAXS patterns for azimuthal correlations at a certain q value and different correlation angle Δ values according to

$$C(q,\Delta) = \frac{\langle I(q,\phi)I(q,\phi+\Delta)\rangle_\phi - \langle I(q,\phi)\rangle_\phi^2}{\langle I(q,\phi)\rangle_\phi^2},$$

where ϕ is the azimuth angle of a 2D scattering pattern. In the case of a crystalline material, such as an ordered nanocrystal superlattice, the choice of the q value is typically determined by the position of the Bragg peaks. Especially for the first strongest Bragg peaks of the superlattice, well-resolved correlations can be obtained.[43]

The analysis of the Fourier coefficients of the correlation function $C(q,\Delta)$ enables access to the qualitative measures of the symmetry of a 2D scattering pattern.[44] In the case of Bragg reflections, the fourth (C_4) and the sixth (C_6) Fourier coefficients exhibit the highest values if the angle between equivalent lattice planes corresponds to 90° and 60°, respectively (**Figure S5**). Interestingly, the azimuthally integrated SAXS curves at 37.43 – 48.41 min (Figure 4a) could be modeled using both the BCC phase emerging from the HCP phase as well as the FCC superstructure (**Figure 4b, c**). The XCCA approach to the data evaluation at 37.43 min to 48.41 min confirms the coexistence of HCP and BCC phases through comparison of the experimentally observed values of the C_4 and C_6 Fourier coefficients (**Figure 4d, e**) with the expected contributions to the C_4 and C_6 components for the assumed lattice structures (HCP/BCC or FCC) with the corresponding Bragg reflections (see **Figure S5** and **Table S1**). Thus, by means of XCCA the formation of the BCC phase from

the hexagonal phase can be unambiguously revealed (see Table S1 and discussion in the Supporting Information). This demonstrates the importance of the XCCA, where the two-dimensional information from scattering patterns can be extracted at a higher extent without loss due to averaging.

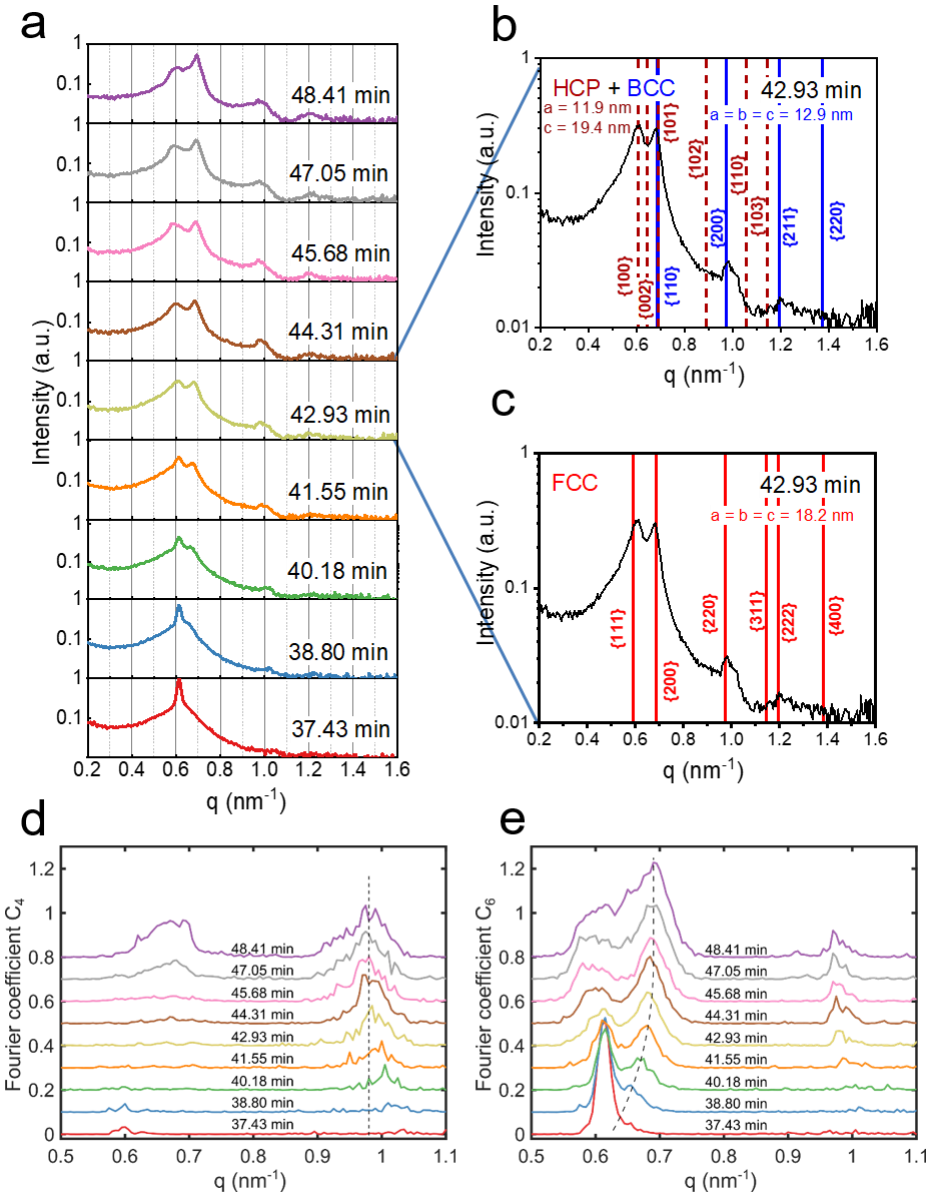

Figure 4. Evolution of the cubic superlattice phase from the hexagonal ordering: (a) Time-resolved azimuthally integrated SAXS curves during the *in situ* self-assembly of PbS NCs from 37.43 to 48.41 min after the start of solvent evaporation. (b), (c) Modeling of the SAXS curve at 42.93 min

of elapsed time by a mixture of the HCP and BCC superlattice phases as well as by the FCC superlattice phase, respectively. (d), (e) The fourth C_4 and the sixth C_6 Fourier coefficients obtained from the XCCA of two-dimensional SAXS patterns for the same assembly times as the azimuthally integrated SAXS curves in (a), respectively. The dotted lines in (d) and (e) show the evolving contributions from reflections of the BCC superlattice, *i.e.*, $\{110\}_{\mathrm{BCC}}$ in (e) and $\{200\}_{\mathrm{BCC}}$ in (d).

Later on, the BCC superlattice undergoes a tetragonal distortion resulting in a BCT superlattice with lattice constants $a = b = 12.6$ nm and $c = 13.2$ nm at 66.29 min of elapsed time and further $a = b = 12.4$ nm and $c = 13.6$ nm at 78.78 min (Figure 3). This is again in agreement with our previous study performed with a different NC batch measured in a different experiment.[28] For this particular measurement, the solvent evaporation from the remaining bulk colloidal suspension and thus from the swollen self-assembled superlattice starts at approx. 89 min of elapsed time. The detection of this temporal point is possible due to the simultaneous measurements over different vertical positions on the cell windows.[31] The SAXS curve at 89.90 min (not shown here) can be best modeled by a mixture of two coexisting BCT superlattices with lattice constants of $a = b = 12.2$ nm and $c = 13.8$ nm (more pronounced) as well as $a = b = 10.4$ nm and $c = 13.8$ nm (less pronounced). During further solvent evaporation, at 92.68 min of elapsed time (not shown here) the BCT superlattice with $a = b = 10.4$ nm and $c = 13.8$ nm becomes predominant and the BCT superlattice with $a = b = 12.2$ nm and $c = 13.8$ nm diminishes. At 99.65 min, the superlattice is dried with no further signs of the solvent evaporation and can be described as the BCT phase with $a = b = 10.4$ nm and $c = 13.8$ nm (Figure 3) with some fraction of the FCC phase with $a = b = 9.9$ nm and $c = 14.0$ nm present (**Figure S6**). In the latter case, the unit cell axes are referred to the BCC unit cell, meaning that the FCC lattice meets the condition $c = \sqrt{2} \cdot a$. Otherwise, using a more common description of the FCC lattice with three equal lattice axes,

the Bragg reflections shown in Figure S6 for the FCC phase correspond to $a_1 = b_1 = c = 14.0$ nm. The detailed analysis of the larger mesh acquired on the final dried superlattice shown in Figure 2b revealed the average value of the lattice constant a = 10.2 ± 0.4 nm, resulting in a nearest neighbor distance of 9.98 ± 0.16 nm for the BCT structure and 9.88 ± 0.14 nm for the FCC structure.

The structural behavior of the time-resolved superlattice transitions and the phase coexistence shown in Figure 2c and Figure 3 is summarized in Scheme 1.

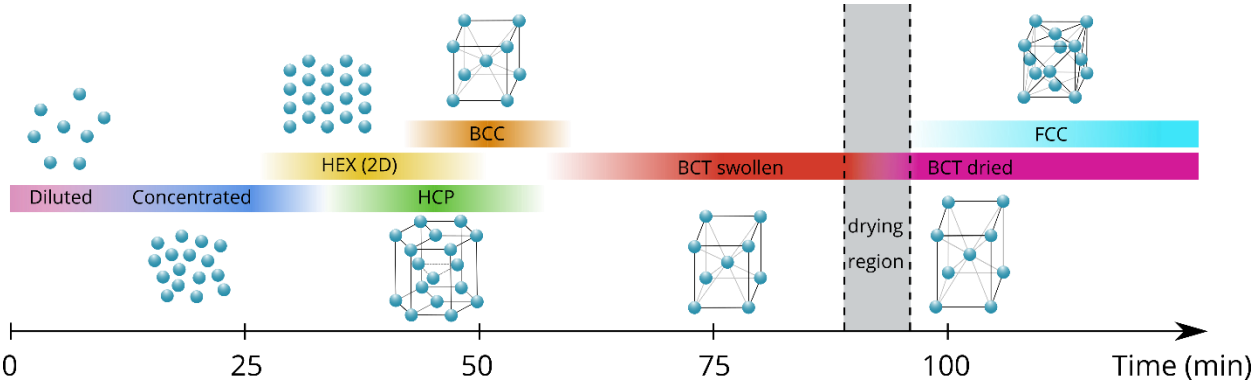

Scheme 1. Evolution of intermediate phases during the *in situ* self-assembly with evaporation time. The color gradient shows the emergence or disappearance of a corresponding superlattice structure.

The final BCT phase has a c/a ratio of 1.33, which is close to the c/a ratio of $\sqrt{2}$ describing the FCC phase. Thus, upon solvent evaporation the PbS NCs in this study form a BCT superlattice which approaches and partly results in the FCC one. The BCC to FCC transition through intermediate BCT structures is described by the Bain path in martensite steel[45] and has been recently observed for PbS and PbSe NC superlattices upon solvent evaporation.[9,15,16] The Bain deformation from the BCC to the FCC lattice occurs through expansion of the c-axis by $2^{1/3}$and

contraction of the a, b-axes by $2^{-1/6}$, whereas the volume of the lattice remains constant.[46] **Figure 5a** shows the time-resolved lattice constant values of the a, b-axes and the c-axis during the structural transitions from the BCC through the BCT to the FCC superlattice. As it can be seen from **Figure 5b**, the volume of the superlattice does not change substantially during the transition from BCC to BCT in the solvated state, whereas the values of the a, b-axes and the c-axis change with solvent evaporation. After the solvent evaporation from the bulk suspension and from the swollen superlattice voids, the volume reduces by about 27%. The same trend is observed for the nearest-neighbor distance, defined as $NN = \frac{\sqrt{(a^2+b^2+c^2)}}{2}$ for the general case of a body-centered orthorhombic lattice, which does not change significantly during the BCC to BCT transformation in the solvated superlattice (**Figure 5c**).

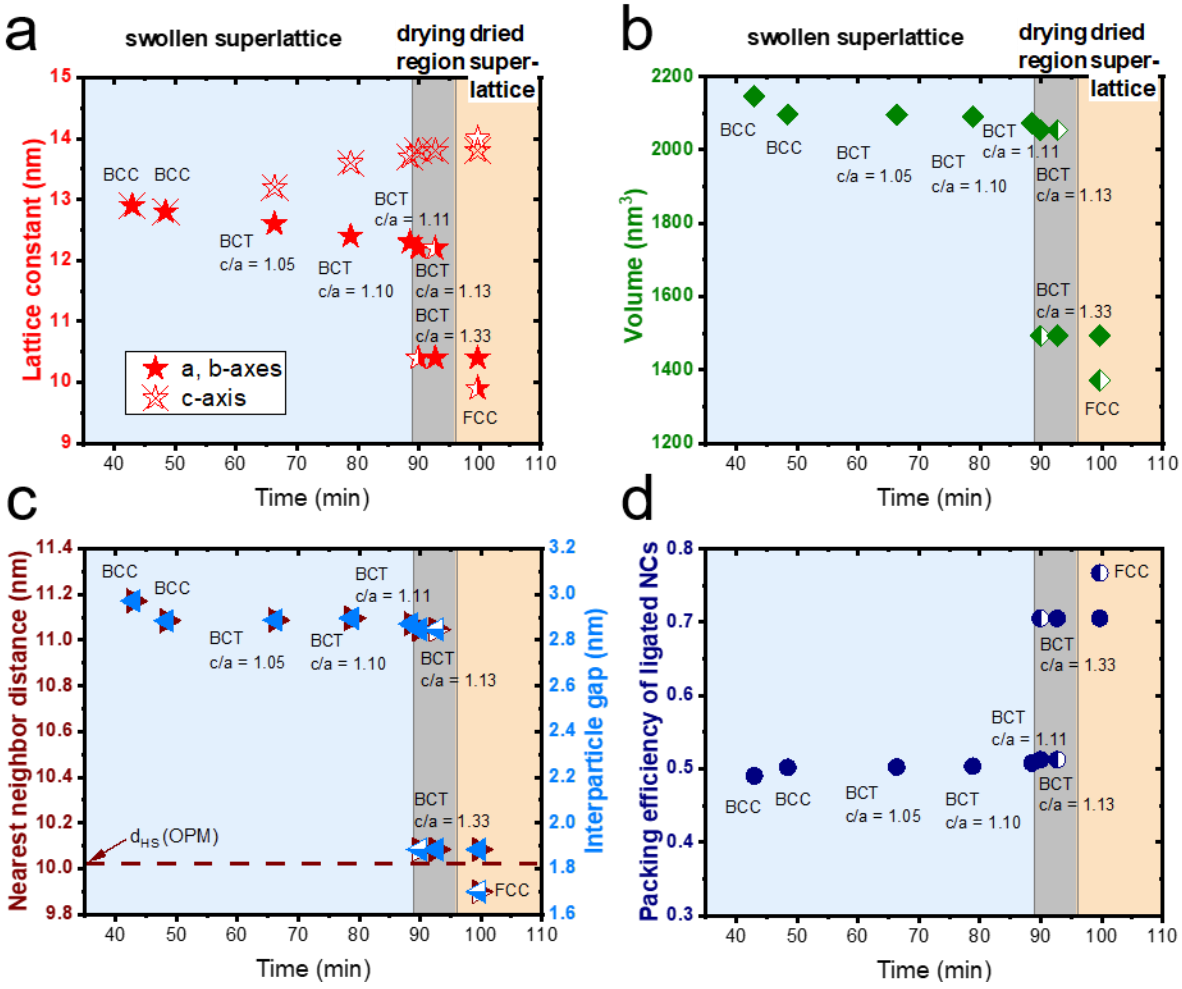

Figure 5. Analysis of different parameters within the cubic phase transitions. Evaluation of the hexagonal phase preceding the BCC superlattice (see Figure 3 and Scheme 1) is not shown in these figures for simplicity. (a) Time-resolved lattice constants for the self-assembled BCC, BCT, and FCC superlattices describing the SAXS curves shown in Figure 3. (b) Volume of the superlattice calculated from the lattice constant values shown in (a). (c) Time-resolved values of the nearest neighbor distance in the self-assembled BCC, BCT, and FCC superlattices (triangles pointing right) calculated from the SAXS curves shown in Figure 3 and the corresponding interparticle separation values (triangles pointing left). The dashed horizontal line shows the hard sphere diameter of ligated NCs for the final NC superlattice calculated using the OPM formula. (d) Packing efficiency of PbS NCs with consideration of the ligand corona, calculated assuming a spherical NC core. For all subfigures, the full-colored points show the predominant structures at the corresponding assembly stage, whereas the half-colored points describe the less pronounced

phases. In (a) the *c*-axis values are denoted with the crossed star symbols for the BCC/BCT phases (the *c*-axis values are the same both for the predominant and the less pronounced BCT phases in the drying region) and the colorless star symbol for the FCC phase. The blue region in the graph background corresponds to the superlattice in the swollen state. The gray region shows the time period during which the final solvent evaporation from the bulk suspension and hence from the swollen superlattice film, assembled along the cell windows, takes place. The orange region describes the state of the dried superlattice. The cubic superlattice structures are indicated at the corresponding points for better visualization according to the analysis in Figure 3, which depicts several chosen times.

To keep the nearest-neighbor distance constant, the second nearest neighbor distance, which corresponds to the length of the a-axis in both BCC and BCT lattices, gradually decreases from 12.8 nm in BCC to 12.6 nm (and later to 12.2 nm) in BCT, whereas the c-axis slightly increases (Figure 5a). At 48.41 min of evaporation time, where the second-nearest neighbor distance is 12.8 nm, the interparticle separation of 4.6 nm between the second nearest neighbors corresponds to the double length of the oleic acid molecule (~2.29 nm[47]). After the superstructure has dried, at 99.65 min of elapsed time the BCT superlattice exhibits an a, b-axes lattice constant of 10.4 nm, resulting in a second-nearest neighbor gap of 2.2 nm and thus approximately a single oleic acid molecule distance. From these observations it is evident that there is a certain interaction between the second-nearest neighbor particles, which acts as a driving force for the assembly pathway, confirming the reported model in ref 48 where the BCT lattice is proposed to be stabilized by the balanced ligand-ligand interactions between adjacent $\{111\}_{PbS}$-$\{111\}_{PbS}$ and $\{100\}_{PbS}$-$\{100\}_{PbS}$ facets.

By comparing these observations to our previous findings in ref 28, where the final BCT superlattice exhibited a c/a ratio of 1.17, we conclude that the ligand grafting density influences the degree of tetragonal distortion in oleic acid-capped PbS NC superlattices and the observed

structural differences are caused by differences in the ligand-induced interactions between adjacent particles. The higher ligand coverage of oleic acid molecules on the PbS NC core (*i.e.*, 4.5 chains/nm^2 considering a cuboctahedral core shape) leads to the lower c/a ratio in a BCT structure,[28] whereas the lower oleic acid grafting density (*i.e.*, 2.7 chains/nm^2 considering a cuboctahedral core shape) results in the higher c/a ratio and thus the FCC(-like) structure. The lower ligand coverage is expected to increase the anisotropy of the ligand corona due to the different binding energy of oleic acid molecules to the $\{100\}_{\mathrm{PbS}}$ and $\{111\}_{\mathrm{PbS}}$ facets.[26] Additionally, it has been demonstrated by molecular dynamics simulations that for the 7 nm sized PbS NCs capped with oleic acid at a low ligand coverage (1.8–3.6 chains/nm^2) the ligand distribution is asymmetric around the NC core resulting in ligand-depleted regions in the interstitial sites between adjacent NCs.[49] This is confirmed by our experiment, where we observe a closer distance between the nearest neighbors and the second-nearest neighbor particles for ligand-deficient PbS NCs. Thus, in this study, the interparticle gap between the nearest neighbor particles in the final BCT superlattice is $NN - d_{NC} \approx 1.9$ nm (Figure 5c). For comparison, for ligand-rich PbS NCs,[28] the separation between the nearest neighbor particles was slightly larger ~2.0 nm.

Much larger differences are observed for the separation between the second nearest neighbors, *i.e.*, 2.2 nm for the final BCT after drying (c/a = 1.33) for the case of PbS NCs with the lower ligand coverage *versus* 2.9 nm for the final dried BCT superlattice (c/a = 1.17) for PbS NCs with the higher ligand coverage[28] indicating emergence of stronger interactions between the second nearest neighbor particles. These observations are in accordance with the increase of the coordination number during the transition from a BCC to an FCC lattice through tetragonal distortion. We note that this conclusion is valid for the investigated core diameters of approx. 7.8–8.2 nm with the softness values of 0.56–0.59 ($\frac{\text{length of oleic acid molecule (nm)}}{\text{NC core radius (nm)}} = \frac{2.29}{3.9 \text{ or } 4.1}$) and could be different for

smaller or larger NC sizes (which would exhibit different shapes and different softness values for the same capping ligand). This observation provides a possible explanation for the variety of structures reported for the superlattices in a dried state obtained from the evaporation-induced assembly of similarly sized oleic acid-functionalized PbS NCs, such as *e.g.*, the FCC or BCT with different degree of tetragonal distortion.[13,50-52]

Calculating the hard sphere diameter (see ref 53) of ligated PbS NCs used in this study according to the optimal packing model (OPM)[54] formula $d_{HS} = D(1 + 3\lambda\xi)^{1/3}$, where $\lambda = \frac{2L}{D}$ (L is the fully extended length of the ligand and D is the core diameter) and $\xi = \sigma/\sigma_{max}$ (σ is the ligand grafting density and σ_{max} is the maximum possible ligand grafting density for a given molecule), we obtain d_{HS} = 10.02 nm (where L = 2.29 nm, σ = 2.7 ligands/nm^2, σ_{max} = 5.5 ligands/nm^2 (see ref 47)). The hard sphere diameter of the nanoparticles is an important parameter which in the case of ligand-coated nanocrystals is involved in theoretical calculations that predict the deformation of the ligand shell.[47,55] According to ref 53, the value of the hard sphere diameter of nanoparticles can be experimentally obtained as the nearest neighbor FCC distance for single component assemblies. In our case, the comparison of the calculated d_{HS} by means of the OPM formula using the ligand grafting density determined by the TGA results is in a reasonably good agreement with the nearest neighbor distance values obtained for the dried BCT, *i.e.*, 10.08 nm, and the dried FCC, *i.e.*, 9.9 nm, superlattices (Figure 5c). Based on the estimated ligand coverage, we have calculated the packing efficiency of ligated nanocrystals, assuming both a spherical and cuboctahedral shape of the inorganic core, during the assembly process (**Figure 5d** and **Figure S7**) (for details of the calculations see Supporting Information).

According to ref 56, the crystallization of the superlattice from ligand-coated nanocrystals by solvent evaporation in equilibrium is initiated when the packing fraction reaches the hard-sphere

liquid–solid transition η_{HS}^{f} = 0.49. Intriguingly, in our *in-situ* experiment at 42.93 min of elapsed time, when the BCC structure can be undoubtedly determined from the hexagonal phase (Figure 4a), the packing efficiency of the BCC superlattice based on the calculations considering a spherical NC core and taking into account the ligand corona is 0.49 (Figure 5d). This observation allows us to assume that the BCC phase is formed from the HCP phase when the evaporation front moves below the measurement point, caused by an increase of the volume fraction of nanoparticles. In other words, we suggest that the HCP superlattice exists when the superlattice is in a strongly solvated state, meaning that the bulk solvent is in direct contact with the self-assembled superstructure. During further solvent evaporation, the evaporation front moves downwards in the sample cell and the number of solvent molecules within the swollen superlattice reduces. At this point the superlattice transforms to the weaker solvated state (with still some solvent molecules trapped within the ligands) resulting in the formation of the BCC superlattice.

This subtle distinguishing between the "strongly" and "weakly" solvated states is possible because of the relatively large NC size resulting in pronounced faceting of the core with a low softness value. Thus, the ligand corona of the newly formed self-assembled superlattice is completely swollen by solvent molecules and effectively masks the polyhedral shape of the inorganic core leading to a more spherical NC core-ligand system and hence an HCP superlattice. However, as the evaporation front moves downwards and the NC volume fraction increases at a particular measurement point, the anisotropy of the entire inorganic core/organic shell system starts to play a role causing the formation of the BCC superlattice. The BCC structure was shown to be energetically favored over the FCC one due to more efficient ligand interactions on the second-nearest neighbor particles for the case of sufficiently long ligands.[54,57-59] Furthermore, a recent theoretical study predicted an FCC to BCC superlattice transition with decreasing solvent content

driven mainly by changes in the translational entropy of the solvent, which stabilized the BCC structure for low solvent content fractions.[60] Additionally, the ligand packing frustration may play a role in the formation of the BCC lattice, because the shape of the Wigner–Seitz cell in BCC places less of entropic penalty on the ligand distribution (compared, *e.g.*, with the FCC phase).[61] In the weakly solvated state, upon continuous solvent evaporation, the packing fraction of the cubic phase increases marginally up to 0.51 in the solvent vapor saturated atmosphere (Figure 5d). After drying of the superlattice, when the bulk solvent in the colloidal suspension and hence the trapped solvent molecules within the solvated superlattice film evaporate the packing efficiency reaches 0.71 for the final BCT phase (c/a ratio of 1.33), which is in good agreement with the packing fraction expected for hard spheres of 0.72 given by $f = \frac{\pi}{24} \cdot \frac{1}{c/a}[(c/a)^2 + 2]^{3/2}$.[62]

For the FCC fraction, the obtained packing parameter is 0.76 and thus higher than theoretically possible for hard spheres, which could be a result of the subtle NC rearrangement in respect to the size dispersity and/or ligand compression or rearrangement within the superlattice caused by the shrinkage stress upon solvent evaporation.[63] The changes in the ligand corona upon drying are evident from a very narrow interparticle gap between both the nearest neighbor particles and the second nearest neighbors, both equal to 1.7 nm. The shorter interparticle distances than a fully-extended ligand length could be a result of a suggested tendency of ligands to lay flat against the NC surface forming a "wet hair" model[64] or attaining a "mushroom" configuration through bending of the chains that were previously stretched out.[65] In the solvated superlattice state, the solvent molecules penetrate the oleic acid ligands, which preferentially attach to the $\{111\}_{NC}$ facets, and might additionally reside in the close proximity to the $\{100\}_{NC}$ facets, where void space is left by ligands. The effective reduction of the shell thickness upon deswelling could probably lead to higher packing densities as it is known for other soft systems.[66] Considering experimental

uncertainties in the determination of the ligand grafting density (2.71 ± 0.27 chains/nm^2) and lattice parameters during the *in situ* self-assembly, we find that there is an excellent agreement between experimental results and theoretical predictions. For completeness, Figure S7 depicts the packing efficiency obtained for the assumption of a cuboctahedral shape of the core leading to substantially lower values, as expected.

CONCLUSIONS

To conclude, we performed the *in situ* self-assembly of colloidal PbS NCs into superlattices upon controlled solvent evaporation by means of SAXS in the transmission geometry and XCCA. We observed the structural diversity of time-resolved transitions during the slow change of the solvent/NC volume fraction and determined at the beginning of the self-assembly a so called "strongly" solvated state (the HEX 2D and later the HCP superlattice) followed by a "weakly" solvated state (the BCC superlattice). During further solvent evaporation, the BCC superlattice underwent transformation into the BCT one, still being in a swollen state. Upon drying, the BCT structure was found to exhibit a rather high degree of tetragonal distortion close to the FCC (with a small fraction of the FCC structure present). Thus, in a single self-assembly experiment we have observed a large variety of different superlattice structures, *i.e.*, the HEX 2D, HCP, BCC, BCT (with different c/a ratios), and the FCC, caused by the controlled solvent evaporation under quasi equilibrium conditions.

Comparing the results obtained in this paper with the findings from ref 28, the role of the ligand grafting density on the degree of tetragonal distortion in the BCT superlattice could be explicitly deduced. Ligand-deficient PbS NCs (grafting density of 2.7 molecules/nm^2) form the BCT

superlattice with a larger degree of tetragonal distortion (c/a = 1.33) which is close to the FCC one, whereas ligand-rich PbS NCs (grafting density of 4.5 molecules/nm^2) self-assemble into the BCT superstructure with a lower degree of tetragonal distortion (c/a = 1.17). The driving force for the larger tetragonal distortion was found to be caused by interactions between second nearest neighbor NCs, which are located at the distance of the a-axis both for the BCC and BCT superlattices. This result demonstrates the importance of the determination of the degree of ligand coverage in assembly experiments, especially in view of possible comparison of structures obtained in different laboratories. Furthermore, the ligand density represents a crucial parameter that has to be known for the modelling of the assembly process and thus is encouraged to be determined in every self-assembly experiment.

Despite the at first sight apparent simplicity of the single component NC assemblies, especially based on well-investigated nanoparticle sample systems, such as, *e.g.*, oleic acid-capped PbS NCs, we are still far from a complete understanding of the driving forces governing the assembly pathway. In this respect, a broader application of *in situ* measurement methods (*e.g.*, scattering, electron microscopy imaging *etc.*) emerging in the recent years should contribute substantially to the acquisition of additional knowledge in the field of nanocrystal assembly, which would be as well beneficial for more complicated systems, such as binary NC superlattices and assemblies from non-spherical shaped nanoparticles.

ACKNOWLEDGMENTS

The authors acknowledge DESY (Hamburg, Germany), a member of the Helmholtz Association HGF, for the provision of experimental facilities. Parts of this research were carried out at PETRA

III (beamtime 11006883) and at the University of Hamburg. The authors thank Michael Sprung for assistance in using P10 beamline, Florian Schulz for assistance with TGA measurements, Andreas Kornowski and Stefan Werner for TEM measurements as well as Robert Schön for SEM measurements.

This work was financially supported by DESY, a member of the Helmholtz Association (HGF), and by the Cluster of Excellence "Advanced Imaging of Matter" of the Deutsche Forschungsgemeinschaft (DFG) – EXC 2056 – project ID 390715994.

ASSOCIATED CONTENT

Supporting Information: The Supporting Information is available free of charge via the Internet at http://pubs.acs.org.

Calculation of the evaporation rate during the *in situ* self-assembly; determination of the ligand grafting density using the thermogravimetric analysis; optical microscopy images of the dry self-assembled superlattice film; SAXS curves from 29.15 min until 37.43 min after start of evaporation; X-ray cross correlation analysis of the two-dimensional SAXS patterns; detailed analysis of the superlattice at 99.65 min; and calculation of the packing efficiency of ligated nanocrystals (PDF)

AUTHOR INFORMATION

Corresponding Author

*E-mail: irina.lokteva@desy.de

Notes

The authors declare no competing financial interest.

REFERENCES

(1) Boles, M. A.; Engel, M.; Talapin, D. V. Self-Assembly of Colloidal Nanocrystals: From Intricate Structures to Functional Materials. *Chem. Rev.* **2016**, 116, 11220–11289.

(2) Li, X.; Liu, X.; Liu, X. Self-assembly of colloidal inorganic nanocrystals: nanoscale forces, emergent properties and applications. *Chem. Soc. Rev.*, **2021**, 50, 2074–2101.

(3) Lee, H.; Yoon, D.-E.; Koh, S.; Kang, M. S.; Lim, J.; Lee, D. C. Ligands as a universal molecular toolkit in synthesis and assembly of semiconductor nanocrystals. *Chem. Sci.*, **2020**, 11, 2318–2329.

(4) You, H. R.; Park, J. Y.; Lee, D. H.; Kim, Y.; Choi, J. Recent Research Progress in Surface Ligand Exchange of PbS Quantum Dots for Solar Cell Application. *Appl. Sci.* **2020**, 10, 975.

(5) Hetsch, F.; Zhao, N.; Kershaw, S. V.; Rogach, A. L. Quantum Dot Field Effect Transistors. *Mater. Today* **2013**, 16, 312–325.

(6) Singh, S.; Leemans, J.; Zaccaria, F.; Infante, I.; Hens, Z. Ligand Adsorption Energy and the Postpurification Surface Chemistry of Colloidal Metal Chalcogenide Nanocrystals. *Chem. Mater.* **2021**, 33, 2796–2803.

(7) Weir, M. P.; Toolan, D. T. W.; Kilbride, R: C.; Penfold, N. J. W.; Washington, A. L.; King, S. M.; Xiao, J.; Zhang, Z.; Gray, V.; Dowland, S.; Winkel, J.; Greenham, N. C.; Friend, R. H.; Rao, A.; Ryan, A. J.; Jones, R. A. L. Ligand Shell Structure in Lead Sulfide–Oleic Acid Colloidal Quantum Dots Revealed by Small-Angle Scattering. *J. Phys. Chem. Lett.* **2019**, *10*, 4713–4719.

(8) Weidman, M. C.; Nguyen, Q.; Smilgies, D.-M., Tisdale, W. A. Impact of Size Dispersity, Ligand Coverage, and Ligand Length on the Structure of PbS Nanocrystal Superlattices. *Chem. Mater.* **2018**, 30, 807–816.

(9) Choi, J. J.; Bealing, C. R.; Bian, K.; Hughes, K. J.; Zhang, W.; Smilgies, D.-M.; Hennig, R. G.; Engstrom, J. R.; Hanrath, T. Controlling Nanocrystal Superlattice Symmetry and Shape-Anisotropic Interactions through Variable Ligand Surface Coverage. *J. Am. Chem. Soc.* **2011**, 133, 3131–3138.

(10) Bian, K.; Li, R.; Fan, H. Controlled Self-Assembly and Tuning of Large PbS Nanoparticle Supercrystals. *Chem. Mater.* **2018**, 30, 6788–6793.

(11) Wang, Z.; Schliehe, C.; Bian, K.; Dale, D.; Bassett, W. A.; Hanrath, T.; Klinke, C.; Weller, H. Correlating Superlattice Polymorphs to Internanoparticle Distance, Packing Density, and Surface Lattice in Assemblies of PbS Nanoparticles. *Nano Lett.* **2013**, 13, 1303–1311.

(12) Zaluzhnyy, I. A.; Kurta, R. P.; André, A.; Gorobtsov, O. Y.; Rose, M.; Skopintsev, P.; Besedin, I.; Zozulya, A. V.; Sprung, M.; Schreiber, F.; Vartanyants, I. A.; Scheele, M. Quantifying Angular Correlations between the Atomic Lattice and the Superlattice of Nanocrystals Assembled with Directional Linking. *Nano Lett.* **2017**, 17, 3511–3517.

(13) Mukharamova, N.; Lapkin, D.; Zaluzhnyy, I. A.; André, A.; Lazarev, S.; Kim, Y. Y.; Sprung, M.; Kurta, R. P.; Schreiber, F.; Vartanyants, I. A.; Scheele, M. Revealing Grain Boundaries and Defect Formation in Nanocrystal Superlattices by Nanodiffraction. *Small* **2019**, 15, 1904954.

(14) Maier, A.; Lapkin, D.; Mukharamova, N.; Frech, P.; Assalauova, D.; Ignatenko, A.; Khubbutdinov, R.; Lazarev, S.; Sprung, M.; Laible, F.; Löffler, R.; Previdi, N.; Bräuer, A.;

Günkel, T.; Fleischer, M.; Schreiber, F.; Vartanyants, I. A.; Scheele, M. Structure–Transport Correlation Reveals Anisotropic Charge Transport in Coupled PbS Nanocrystal Superlattices. *Adv. Mater.* **2020**, 32, 2002254.

(15) Bian, K.; Choi, J. J.; Kaushik, A.; Clancy, P.; Smilgies, D.-M.; Hanrath, T. Shape-Anisotropy Driven Symmetry Transformations in Nanocrystal Superlattice Polymorphs. *ACS Nano* **2011**, 5, 2815–2823.

(16) Weidman, M. C.; Smilgies, D.-M.; Tisdale, W. A. Kinetics of the self-assembly of nanocrystal superlattices measured by real-time *in situ* X-ray scattering. *Nat. Mater.* **2016**, 15, 775–781.

(17) Liu, L.; Bisri, S. Z.; Ishida, Y.; Aida, T.; Iwasa, Y. Tunable electronic properties by ligand coverage control in PbS nanocrystal assemblies. *Nanoscale*, **2019**, 11, 20467–20474.

(18) Zherebetskyy, D.; Scheele, M.; Zhang, Y.; Bronstein, N.; Thompson, C.; Britt, D.; Salmeron, M.; Alivisatos, P.; Wang, L.-W. Hydroxylation of the surface of PbS nanocrystals passivated with oleic acid. *Science* **2014**, 344, 1380–1384.

(19) Boles, M., Ling, D., Hyeon, T., Talapin, D. V. The surface science of nanocrystals. *Nature Mater.* **2016**, 15, 141–153.

(20) Beygi, H.; Sajjadi, S. A.; Babakhani, A.; Young, J. F.; van Veggel, F. C. J. M. Surface chemistry of as-synthesized and air-oxidized PbS quantum dots. *Appl. Surf. Sci.* **2018**, 457, 1–10.

(21) Bealing, C.R.; Baumgardner, W.J.; Choi, J.J.; Hanrath, T.; Hennig, R.G. Predicting Nanocrystal Shape through Consideration of Surface-Ligand Interactions. *ACS Nano* **2012**, 6, 2118–2127.

(22) Boles, M. A.; Talapin, D. V. Binary Assembly of PbS and Au Nanocrystals: Patchy PbS Surface Ligand Coverage Stabilizes the CuAu Superlattice. *ACS Nano* **2019**, 13, 5375–5384.

(23) Maiti, S.; André, A.; Banerjee, R.; Hagenlocher, J.; Konovalov, O.; Schreiber, F.; Scheele, M. Monitoring Self-Assembly and Ligand Exchange of PbS Nanocrystal Superlattices at the Liquid/Air Interface in Real Time. *J. Phys. Chem. Lett.* **2018**, 9, 739–744.

(24) Li, T.; Senesi, A. J.; Lee, B. Small Angle X-ray Scattering for Nanoparticle Research. *Chem. Rev.* **2016**, 116, 11128–11180.

(25) Saxena, V.; Portale; G. Contribution of Ex-Situ and In-Situ X-ray Grazing Incidence Scattering Techniques to the Understanding of Quantum Dot Self-Assembly: A Review. *Nanomaterials* **2020**, 10, 2240.

(26) Corricelli, M.; Altamura, D.; Curri, M. L.; Sibillano, T.; Siliqi, D.; Mazzone, A.; Depalo, N.; Fanizza, E.; Zanchet, D.; Giannini, C.; Striccoli, M. GISAXS and GIWAXS study on self-assembling processes of nanoparticle based superlattices. *CrystEngComm*, **2014**, 16, 9482–9492.

(27) Schulz, F.; Lokteva, I.; Parak, W. J.; Lehmkühler, F. Recent Notable Approaches to Study Self-Assembly of Nanoparticles with X-ray Scattering and Electron Microscopy. *Part. Part. Syst. Charact.* **2021**, doi 10.1002/ppsc.202100087.

(28) Lokteva, I.; Koof, M.; Walther, M.; Grübel, G.; Lehmkühler, F. Coexistence of hcp and bct Phases during In Situ Superlattice Assembly from Faceted Colloidal Nanocrystals. *J. Phys. Chem. Lett.* **2019**, 10, 6331–6338.

(29) Hines, M. A.; Scholes, G. D. Colloidal PbS Nanocrystals with Size-Tunable Near-Infrared Emission: Observation of Post-Synthesis Self-Narrowing of the Particle Size Distribution. *Adv. Mater.* **2003**, 15, 1844–1849.

(30) Lokteva, I.; Walther, M.; Koof, M.; Grübel, G.; Lehmkühler, F. *In situ* small-angle X-ray scattering environment for studying nanocrystal self-assembly upon controlled solvent evaporation. *Rev. Sci. Instrum.* **2019**, 90, 036103.

(31) Lokteva, I.; Koof, M.; Walther, M.; Grübel, G.; Lehmkühler, F. Monitoring Nanocrystal Self-Assembly in Real Time Using In Situ Small-Angle X-Ray Scattering. *Small* **2019**, 15, 1900438.

(32) Piliego, C.; Protesescu, L.; Bisri, S. Z.; Kovalenko, M. V.; Loi, M. A. 5.2% efficient PbS nanocrystal Schottky solar cells. *Energy Environ. Sci.* **2013**, 6, 3054–3059.

(33) Tom, A. E.; Thomas, A.; Ison, V. V. Novel post-synthesis purification strategies and the ligand exchange processes in simplifying the fabrication of PbS quantum dot solar cells. *RSC Adv.* **2020**, 10, 30707–30715.

(34) De Roo, J.; Yazdani, N.; Drijvers, E.; Lauria, A.; Maes, J.; Owen, J. S.; Van Driessche, I.; Niederberger, M.; Wood, V.; Martins, J. C.; Infante, I.; and Hens, Z. Probing Solvent–Ligand Interactions in Colloidal Nanocrystals by the NMR Line Broadening. *Chem. Mater.* **2018**, 30, 5485–5492.

(35) Chen, W.; Tang, H.; Li, N.; Scheel, M. A.; Xie, Y.; Li, D.; Körstgens, V.; Schwartzkopf, M.; Roth, S. V.; Wang, K.; Sun, X. W.; Müller-Buschbaum, P. Colloidal PbS quantum dot stacking kinetics during deposition via printing. *Nanoscale Horiz.* **2020**, 5, 880–885.

(36) Schulz, F.; Westermeier, F.; Dallari, F.; Markmann, V.; Lange, H.; Grübel, G.; Lehmkühler, F. Plasmonic Supercrystals with a Layered Structure Studied by a Combined TEM-SAXS-XCCA Approach. *Adv. Mater. Interfaces* **2020**, 7, 2000919.

(37) Huang, X.; Zhu, J.; Ge, B.; Gerdes, F.; Klinke, C.; Wang, Z. In Situ Constructing the Kinetic Roadmap of Octahedral Nanocrystal Assembly Toward Controlled Superlattice Fabrication. *J. Am. Chem. Soc.* **2021**, 143, 4234–4243.

(38) Moody, M. C.; Ray, J. R., Rahman, A. Free energy difference calculations comparing fcc and hcp structures using molecular dynamics computer simulations. *J. Chem. Phys.* **1986**, 84, 1795–1802.

(39) Bolhuis, P.; Frenkel, D.; Mau, S.-C.; Huse, D. A. Entropy difference between crystal phases. *Nature* **1997**, 388, 235–236.

(40) Auer, S.; Frenkel, D. Prediction of absolute crystal-nucleation rate in hard-sphere colloids. *Nature* **2001**, 409, 1020–1023.

(41) Hu, C. H.; Chen, Y. C.; Yu, P. J.; Fung, K. Y.; Hsueh, Y. C.; Liaw, P. K.; Yeh, J. W.; Hu, A. From symmetry to entropy: Crystal entropy difference strongly affects early stage phase transformation. *Appl. Phys. Lett.* **2019**, 115, 264103.

(42) Wochner, P.; Gutt, C.; Autenrieth, T.; Demmer, T.; Bugaev, V.; Ortiz, A. D.; Duri, A.; Zontone, F.; Grübel, G.; Dosch, H. X-ray cross correlation analysis uncovers hidden local symmetries in disordered matter. *Proc. Natl. Acad. Sci. U S A* **2009**, 106, 11511–11514.

(43) Lehmkühler, F.; Fischer, B.; Müller, L.; Ruta, B.; Grübel, G. Structure beyond pair correlations: X-ray cross-correlation from colloidal crystals *J. Appl. Cryst.* **2016**, 49, 2046–2052.

(44) Lehmkühler, F.; Grübel, G.; Gutt, C. Detecting orientational order in model systems by X-ray cross-correlation methods. *J. Appl. Cryst.* **2014**, 47, 1315–1323.

(45) Bain, E. C.; Dunkirk, N. Y. The nature of martensite. *Trans. Am. Inst. Min. Metall. Eng.* **1924**, 70, 25–47.

(46) Kiyokawa, S. Energy barrier of bcc-fcc phase transition via the Bain path in Yukawa system. *Phys. Plasmas* **2018**, 25, 053703.

(47) Travesset, A. Soft Skyrmions, Spontaneous Valence and Selection Rules in Nanoparticle Superlattices. *ACS Nano* **2017**, 11, 5375–5382.

(48) Novák, J.; Banerjee, R.; Kornowski, A.; Jankowski, M.; André, A.; Weller, H.; Schreiber, F.; Scheele, M. Site-Specific Ligand Interactions Favor the Tetragonal Distortion of PbS Nanocrystal Superlattices. *ACS Appl. Mater. Interfaces* **2016**, 8, 22526–22533.

(49) Patra, T. K.; Chan, H.; Podsiadlo, P.; Shevchenko, E. V.; Sankaranarayanan, S. K. R. S.; Narayanan, B. Ligand dynamics control structure, elasticity, and high-pressure behavior of nanoparticle superlattices. *Nanoscale* **2019**, 11, 10655–10666.

(50) Wang, Z.; Bian, K.; Nagaoka, Y.; Fan, H.; Cao, Y. C. Regulating Multiple Variables to Understand the Nucleation and Growth and Transformation of PbS Nanocrystal Superlattices. *J. Am. Chem. Soc.* **2017**, 139, 14476–14482.

(51) Maiti, S.; André, A.; Maiti, S.; Hodas, M.; Jankowski, M.; Scheele, M.; Schreiber, F. Revealing Structure and Crystallographic Orientation of Soft Epitaxial Assembly of Nanocrystals by Grazing Incidence X-ray Scattering. *J. Phys. Chem. Lett.* **2019**, 10, 6324–6330.

(52) Li, R.; Bian, K.; Hanrath, T.; Bassett, W. A.; Wang, Z. Decoding the Superlattice and Interface Structure of Truncate PbS Nanocrystal-Assembled Supercrystal and Associated Interaction Forces. *J. Am. Chem. Soc.* **2014**, 136, 12047–12055.

(53) Zha, X.; Travesset, A. The hard sphere diameter of nanocrystals (nanoparticles). *J. Chem. Phys.* **2020**, 152, 094502.

(54) Landman. U.; Luedtke, W. D. Small is different: energetic, structural, thermal, and mechanical properties of passivated nanocluster assemblies. *Faraday Discuss.* **2004**, 125, 1–22.

(55) Travesset, A. Nanoparticle Superlattices as Quasi-Frank-Kasper Phases. *Phys. Rev. Lett.* **2017**, 119, 115701.

(56) Waltmannn, T.; Travesset, A. Assembly by solvent evaporation: equilibrium structures and relaxation times. *Nanoscale* **2019**, 11, 18702–18714.

(57) Travesset, A. Topological structure prediction in binary nanoparticle superlattices. *Soft Matter* **2017**, 13, 147–157.

(58) Zha, X.; Travesset, A. Stability and Free Energy of Nanocrystal Chains and Superlattices. *J. Phys. Chem. C* **2018**, 122, 23153–23164.

(59) Fan, Z.; Grünwald, M. Orientational Order in Self-Assembled Nanocrystal Superlattices. *J. Am. Chem. Soc.* **2019**, 141, 1980–1988.

(60) Missoni, L. L.; Tagliazucchi, M. The Phase Behavior of Nanoparticle Superlattices in the Presence of a Solvent. *ACS Nano* **2020**, 14, 5649–5658.

(61) Goodfellow, B. W.; Yu, Y.; Bosoy, C. A.; Smilgies, D.-M.; Korgel, B. A. The Role of Ligand Packing Frustration in Body-Centered Cubic (bcc) Superlattices of Colloidal Nanocrystals. *J. Phys. Chem. Lett.* **2015**, 6, 2406–2412.

(62) Dunlap, R. A. The Symmetry and Packing Fraction of the Body Centered Tetragonal Structure. *Eur. J. Phys. Educ.* **2012**, 3, 19–24.

(63) Kapuscinski, M.; Agthe, M.; Lv, Z.-P.; Liu, Y.; Segad, M.; Bergström, L. Temporal Evolution of Superlattice Contraction and Defect-Induced Strain Anisotropy in Mesocrystals during Nanocube Self-Assembly. *ACS Nano* **2020**, 14, 5337–5347.

(64) Geva, N.; Shepherd, J. J.; Nienhaus, L.; Bawendi, M. G.; Van Voorhis, T. Morphology of Passivating Organic Ligands around a Nanocrystal. *J. Phys. Chem. C* **2018**, 122, 26267–26274.

(65) Huerre, A.; Cacho-Nerin, F.; Poulichet, V.; Udoh, C. E.; De Corato, M.; Garbin, V. Dynamic Organization of Ligand-Grafted Nanoparticles during Adsorption and Surface Compression at Fluid–Fluid Interfaces. *Langmuir* **2018**, 34, 1020–1028.

(66) Scotti, A. Characterization of the volume fraction of soft deformable microgels by means of small-angle neutron scattering with contrast variation. *Soft Matter* **2021**,17, 5548-5559.

Table of Contents Graphic